Spectrochimica Acta Part A: Molecular and Biomolecular Spectroscopy 198 (2018) 264–277

Contents lists available at ScienceDirect

Spectrochimica Acta Part A: Molecular and Biomolecular Spectroscopy

journal homepage: www.elsevier.com/locate/saa

IR and NMR spectroscopic correlation of enterobactin by DFT

M. Moreno [a,*], A. Zacarias [b], A. Porzel [c], L. Velasquez [d], G. Gonzalez [e,f], M. Alegría-Arcos [g,h], F. Gonzalez-Nilo [g], E.K.U. Gross [b]

[a] University of the Basque Country, Barrio Sarriena, s/n, 48940 Leioa, Bizkaia, Spain
[b] Max Planck Institute of Microstructure Physics, Weinberg 2, D 06120, Halle, Germany and ETSF
[c] Leibniz Institute of Plant Biochemistry, Weinberg 3, D 06120 Halle, Germany
[d] Universidad Andres Bello, Facultad de Medicina, Center for Integrative Medicine and Innovative Science, Echaurren 183, Santiago, Chile
[e] Center for Development of Nanoscience and Nanotechnology, CEDENNA, Casilla 653, Santiago, Chile
[f] Universidad de Chile, Facultad de Ciencias, Departamento de Química, Laboratorio de Sintesis Inorganica y electroquímica, Las Palmeras 3425, Nuñoa, Santiago, Chile
[g] Universidad Andres Bello, Facultad de Ciencias Biologicas, Center for Bioinformatic and Integrative Biology, Av Republica 239, Santiago, Chile
[h] Centro Interdisciplinario de Neurociencias de Valparaíso (CINV), Facultad de Ciencias, Universidad de Valparaíso, Valparaíso, Chile

ARTICLE INFO

Article history:
Received 19 July 2017
Received in revised form 19 January 2018
Accepted 22 February 2018
Available online 2 March 2018

Keywords:
Enterobactin
NMR
FT-IR
DFT
MALDI-TOF MS

ABSTRACT

Emerging and re-emerging epidemic diseases pose an ongoing threat to global health. Currently, Enterobactin and Enterobactin derivatives have gained interest, owing to their potential application in the pharmaceutical field. As it is known [J. Am. Chem. Soc (1979) 101, 20, 6097–6104], Enterobactin (H_6EB) is an efficient iron carrier synthesized and secreted by many microbial species. In order to facilitate the elucidation of enterobactin and its analogues, here we propose the creation of a H_6EB standard set using Density Functional Theory Infrared (IR) and NMR spectra. We used two exchange-correlation (xc) functionals (PBE including long-range corrections —LC-PBE— and mPW1), 2 basis sets (QZVP and 6-31G(d)) and 2 grids (fine and ultrafine) for most of the H_6EB structures dependent of dihedral angles. The results show a significant difference between the O—H and N—H bands, while the C═O amide and O—(C═O)— IR bands are often found on top of each other. The NMR DFT calculations show a strong dependence on the xc functional, basis set, and grid used for the H_6EB structure. Calculated ^{1}H and ^{13}C NMR spectra enable the effect of the solvent to be understood in the context of the experimental measurements. The good agreement between the experimental and the calculated spectra using LC-PBE/QZVP and ultrafine grid suggest the possibility of the systems reported here to be considered as a standard set. The dependence of electrostatic potential and frontier orbitals with the catecholamide dihedral angles of H_6EB is described. The matrix-assisted laser desorption/ionization time of the flight mass spectrometry (MALDI-TOF MS) of H_6EB is also reported of manner to enrich the knowledge about its reactivity.

1. Introduction

Siderophores in general, are efficient iron carriers synthesized and secreted by microbial species [1,2]. The Siderophore Enterobactin (H_6EB) is a C3-symetric triscatechol composed of a backbone of a trilactone ring and three catecholate units attached through amide linkages (Fig. 1). The catecholate units embed the guest ion in an octahedral cavity, leaving a partially free amide group [1]. Its particular conformation allows a high iron-binding affinity and ion carrier (log K_f: 51) [1]. Catecholates are among nature's most sophisticated structures that are found in granular cuticles of marine mussels, flavonoids, plant enzymes and hormone neurotransmitters. Mimicking these natural structures has led to the synthesis of advanced materials, such as catalytic surfaces, polymeric resins, biosensors, dyes and fuel cells [3,4], as well as modified complex molecules with potential medical applications like the Enterobactin [5,6].

Commonly, all Fe-siderophore complexes require an active protein transport, FepA is a channel protein composed of an N-terminal gate protein and a β-barrel [7]. FepA is connected to an outer membrane receptor (TonB-dependent receptor), which extends into the periplasm. The final step requires the Fe-Enterobactin (FeH_3EB) to be carried through the periplasmic by FepB, which is connected to FepD and FepG cytoplasmic transmembrane proteins, which deliver it through an ATPase to FepC, which provides energy to assist with its uptake through the inner membrane [8,9]. In 2003, R. Chakraborty et al [10] reported that tricatechols are required to be recognized by FepA, making their spectroscopic details relevant for ferric catecholamide analogs of Enterobactin, owing to their potential applications in the pharmaceutical field [11]. Later in 2008, K.N. Raymond [12] illustrate that siderocalin binds both bare and ferric siderophores in order to intercept the delivery of iron to the bacteria, impeding in this manner their virulence.

* Corresponding author.
E-mail address: mmoreno043@ikasle.ehu.eus (M. Moreno).

https://doi.org/10.1016/j.saa.2018.02.060

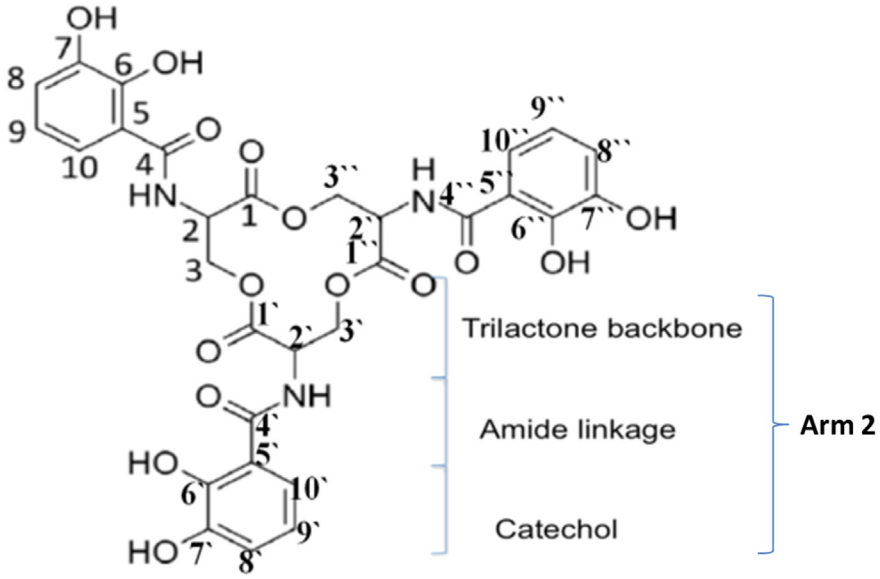

Fig. 1. H_6Enterobactin (H_6EB).

These electrostatic interactions between the siderocalin and the siderophore, regulates the siderophore binding strength.

The lack of a complete description of the H_6EB Infrared (IR) and NMR spectra had led to focus on the description of H_6EB analogues in catechol and amide groups [12,13]. Considering that H_6EB is widely recognized by microorganisms [5–11] and that its strengths as a donor have stimulated extensive studies toward the synthesis of analogs such as SERSAM, TRECAM and TBA7 [5,13], promoting the binding antibiotic molecule to the siderophore (Trojan horse antibiotics strategies), a complete analysis of the experimental IR and NMR spectra correlated by density-functional theory (DFT) calculations will improve the understanding of the reactivity of these systems.

To date, quantum chemical calculations have been used to correlate the experimental UV-Visible results with structural changes in the Enterobactin upon complexation [5,14]. While experimentally IR and NMR spectra are the most useful and accessible spectroscopic characterization tools, DFT IR and NMR calculations are a powerful computational way of exploring the relations among vibrational modes, chemical shifts and molecular structures [15–18].

In this paper we explore as first step in the understanding of the stability and reactivity of iron-siderophores beyond their biological environment, the spectroscopic and electronic properties of H_6EB in order to create an IR and NMR standard set supported by DFT calculations that lead to comprehend at molecular level the experimental spectra of Enterobactin systems. This knowledge implies a better functionalization of Enterobactin-like systems that could not only emulate their biological activity, but also open the possibility of generating a family of systems that allows the control of such reactivity.

In addition, we report the dependence of the NMR and IR spectra, the electrostatic potential and the frontier orbitals with the amide-catechol dihedral angles (Fig. 1, Table 2) of H_6EB. The DFT results presented here, alongside with the MALDI-TOF MS spectra of Enterobactin, also reported here, are an essential part of the study of functionalization of H_6EB and Fe(H_3EB) by vapor phase metalation (VPM) process. The results we have for FeH_3EB will be reported elsewhere.

2. Experimental Details

2.1. Infrared Spectra

Infrared spectra were recorded on a Bruker IFS66v/S vacuum FTIR spectrometer with a Ge/KBr beamsplitter and DTGS detector. For all spectra, 50000, 5000 and 1000 scans recorded at a 2 cm^{-1} resolution were averaged. H_6EB spectra were measured using a KRS-5 disc. Fifty milligrams of H_6EB was dispersed in 100 μl of dichloromethane, then one drop was placed on a KRS-5 disc to dry. Solid H_6EB was characterized. All solvents were of analytical purity and were purchased from Sigma Aldrich.

2.2. NMR Spectra

The 1D (1H, 13C) and 2D (HSQC) NMR spectra were obtained from an Agilent VNMRS 600 system. The spectra were recorded at 599.832 MHz (1H). Chemical shifts were referenced to an internal TMS (δ 0 ppm, 1H), CD3OD (δ 49.0 ppm, 13C) or DMSO-d_6 (δ 39.5 ppm, 13C).

2.3. MALDI-TOF MS

The MALDI-TOF MS spectra were acquired with an Ultraflex II TOF-TOF mass spectrometer (Bruker Daltonics). For the sample preparation, 0.5 ml of a saturated solution of α-cyano-4-hydroxycinnamic acid (HCCA) in acetone was deposited onto the sample target. A 1 ml aliquot of the sample was injected into a small drop of water previously deposited onto the matrix surface.

3. Computational Methods

Quantum Chemical calculations were performed using Density Functional Theory (DFT) with the exchange-correlation (xc) functional

Table 1
Summary of DFT methods.

Short name	xc functional	Basis-set	Grid	Structure
PBE-1	LC-PBE	QZVP	Ultrafine	1
mPW91-1a	mPW91	QZVP	Ultrafine	1
mPW91-1b	mPW91	6-31G(d)	Fine	1
mPW91-1b1	mPW91	6-31G(d)	Ultrafine	1
PBE-2	LC-PBE	QZVP	Ultrafine	2
mPW91-2a	mPW91	QZVP	Ultrafine	2
mPW91-2b	mPW91	6-31G(d)	Fine	2
mPW91-2b1	mPW91	6-31G(d)	Ultrafine	2
PBE-3	LC-PBE	QZVP	Ultrafine	3
PBE-4	LC-PBE	QZVP	Ultrafine	4
PBE-5	LC-PBE	QZVP	Ultrafine	5

Table 2
Dihedral angles of H_6EB structures.

Arm	Labels	Structure-1	Structure-2	Structure-3	Structure-4	Structure-5
1	N-C_4-C_5-C_6	−24.93°	12.26°	−179.95°	−173.50°	2.60°
2	N′-C_4′-C_5′-C_6′	19.50°	11.70°	−179.91°	−173.50°	2.75°
3	N″-C_4″-C_5″-C_6″	127.90°	28.55°	−179.91°	−173.50°	2.75°

PBE including long-range corrections [19], QZVP [20,21] and 6-31G (d) [22,23] basis sets (PBE-1 and PBE-2, respectively). and 2 different grids (fine and ultrafine). Additional results for selected structures using the xc functional mPW91 [19,24–26] are as well presented (mPW91-1 and mPW91-2, respectively), Table 1 summarize the methods, basis sets and grid used, and Table 2 and Fig. 2 show the difference between the dihedral angles from H_6EB structures considered for the calculations. All the results presented correspond to a local minimum for each of the calculated structures. All theoretical results were performed with the Gaussian 09 code [27] and we used Gauss-View to visualize the molecular orbitals, electrostatic potentials and the vibrational modes.

To obtain the frequencies of different dihedral angles values (Arm1, Arm2 and Arm3) from H_6EB structures over a time lapse, molecular dynamics (MD) simulations of the four structures of H_6EB were performed. Then, each structure was embedded, into an explicit TIP3P [28] water box. The NPT ensemble was employed with at 300 K and 1.01 bar of pressure. The OPLS-2005 Force Field [29] was used with Desmond software [30]. Before MD simulations, each system was subjected to energy minimization and then, MD simulations were carried out for 5 ns. We used a VMD software [31] to calculate the dihedrals angles on catecholamides from H_6EB structures during MD trajectory. Plots were done with Origin 6.0 (OriginLab, Northampton, MA). All systems were simulated considering periodic boundary conditions (PBC).

4. Results and Discussion

4.1. H_6EB MALDI-TOF MS Spectra Analysis

The H_6EB spectrum obtained by MALDI-TOF MS analysis is depicted in Fig. 3. Fig. 3 displays different H_6EB fragments, which show a particular tendency toward dissociation in the amide region (—(O═C4)—N, Fig. 1). This tendency could be related to the biosynthesis of H_6EB, which involves the catalysis of an amide linkage between L-serine and 2,3-dihydroxybenzoic acid (DHB) by bifunctional proteins [8], making —(O═C4)—N— a reactive region; this shows the analyte $[H_6EB\text{-}C_7H_5O_3{+}H]^+$ with a 533.833 mass/charge ratio, which matches the calculated value of 533.472 *m/z* (see Table 3). The most abundant isotope localized at 670.118 *m/z* corresponds to $[H_6EB + H]^+$, with a calculated value of 670.593 *m/z*, which is also present in the mixture along with HCCA ($[H_6EB + HCCA]$) at 859.160 *m/z* and Na ($[H_6EB + Na]^+$) at 692.098 *m/z*. Here, HCCA is shown at 189.577 *m/z*, which fits very well with the value of 189.180 *m/z* that was calculated. These results were corroborated by maximum molecular weight based on isotopic abundance

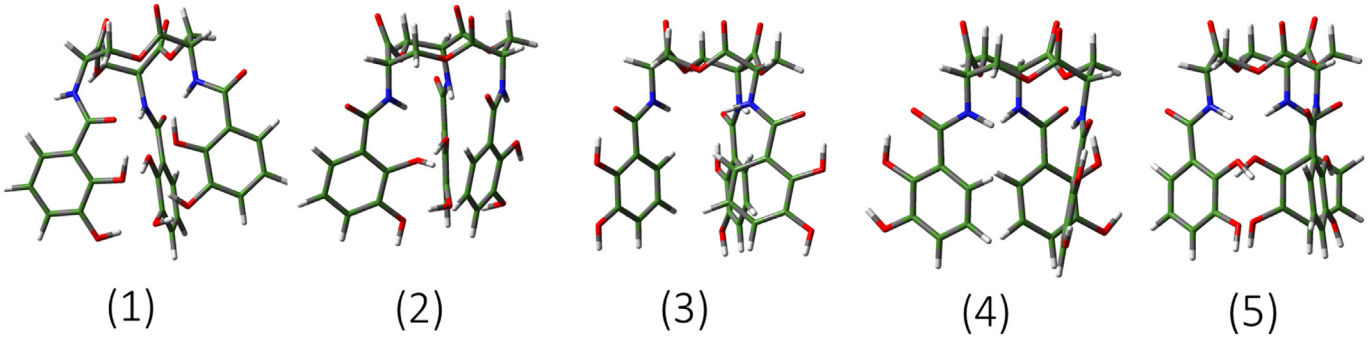

Fig. 2. Structures of H_6EB considered in DFT. All these structures were optimized using the method and basis set as in Table 1 and depicted are the optimized local minimum structures found.

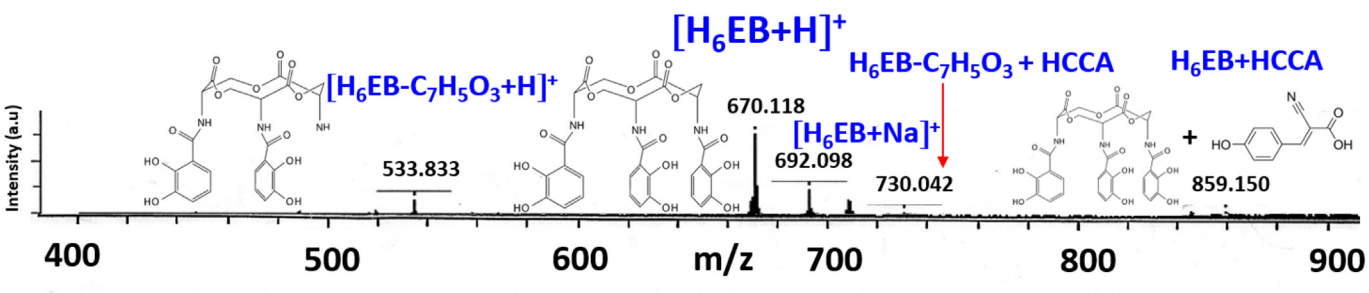

Fig. 3. MALDI-TOF MS spectra of H_6Enterobactin (H_6EB).

Table 3
List of analyte mass/charge ratio of $H_6E{\cdot}B$ and $FeH_3E{\cdot}B$. Elements with a range of atomic weights have been considered using the 2013 technical report from the IUPAC commission on Isotopic Abundances and Atomic Weights [32]. Further structural details can be seen in Fig. S1 of the supplementary information for this paper.

Species	Calculated minimum molecular wt	Calculated maximum molecular wt	Experimental m/z + charge ratio	Max deviation	Sample
[HCCA]	189.154	189.180	189.577	0.423	$H_6E.B$
$[H_6E{\cdot}B]$	669.504	669.585	670.118	0.614	
$[H_6E{\cdot}B + H]^+$	670.513	670.593	670.118	−0.394	
$[H_6E{\cdot}B{-}C_7H_5O_3 + H]^{+a,b}$	533.409	533.472	533.833	0424	
$[H_6E{\cdot}B + Na]^+$	692.494	692.575	692.098	−0.396	
$[H_6E{\cdot}B$ + HCCA]	858.659	858.765	859.160	0.501	

[a] Symbol (−) corresponds to removed fragment.
[b] $C_7H_5O_3$ corresponds to catechol + carbonyl.

and atomic weights from the IUPAC 2013 technical report [32], as shown in Table 3.

4.2. H_6EB NMR Spectra

Fig. 4a shows the ^1H, ^{13}C 2D-HSQC NMR spectra of H_6EB (dissolved in DMSO-d_6). The ^{13}C NMR spectrum shows 10 different signals (see Table 4). The ^1H NMR spectrum shows two OH singlets, one NH doublet, three double doublets for the aromatic protons, two double doublets for the geminal diastereotopic protons H-3A and H-3B and a multiplet for H-2 (see Table 4). The ^1H and ^{13}C chemical shift values are similar to those reported by M. Llinás et al. [33] in DMSO-d_6. Two basis sets (6-31G(d) and QZVP) were used to evaluate the accuracy of the xc-functionals, PBE and mPW91, for these systems using two different grids. The difference between fine and ultrafine grid results, the last computational more expensive, were not as dramatic as the change on the basis set. The results on ^{13}C, ^1H NMR chemical shifts and IR spectra of H_6EB presented to consider the different dihedral angles, hereafter mentioned as structure-1, structure-2, structure-3, structure-4 and structure-5 (see Table 2). Fig. 4b shows the most suitable combination method/basis set (PBE-1/QZVP) for ^{13}C, ^1H 2D NMR spectra, revealing the similitude with experimental result depicted for ^{13}C2,3,8,9,10, and ^1H2,3A,3B,8,9,10 in 2D. The same tendency is displayed for calculated ^{13}C1–10 and ^1H2,3A,3B,8,9,10,6OH,7OH, NH with experimental ^{13}C, ^1H NMR spectra in Fig. 5a, b for PBE-1 instead of other methods, see details in Tables 4 and 5. The shift in the calculated δ value is associated to the H_6EB dynamic, which is influenced by the conditions of the calculation (e.g., gas phase and temperature) and the polarizability of the solvent used [34].

The linear correlation between experimental and calculated ^{13}C and ^1H δ-shifts allows assessing the suitability of the applied calculations methods. In this manner, it is possible to evaluate the effect of the three variables (xc-functional, basis set, and grid, see Table 1) for the calculated H_6EB-structures over the ^{1}HDMSO-d_6 and ^{13}CDMSO-d_6 experimental results (see Tables 5, 6 and 7); so, we consider: (1) xc functional (LC-PBE and mPW91) using the same grid and basis set, (2) large and small basis set (QZVP and 6-31G(d)) using the same grid and (3) the grid (fine and ultrafine) of two H_6EB structures, Fig. 6 summarize R^2 results of whole methods reported in here.

For the H_6EB structure-1; (1) The effect of xc-functional is observed in changes of the ^{13}C signals for the atoms 2, 3, 8, 9 and 10 in the δ-shift region (sensible to the chemical modification), this shows a similar linear correlation for PBE-1 (LC-PBE/QZVP, see Tables 1 and 8) with mPW91-1a. PBE-1 has a slope and correlation factor (R^2) of 0.813 and 0.997, respectively, and a standard deviation (SD) of 2.04 δ (see Fig. 7a) and mPW91-1a of 0.926 and 0.998 using both ultrafine grid and QZVP (see Tables 5 and 8), however when all ^{13}C δ is considered to calculate the linear correlation, mPW91-1a shows better results than PBE-1 (see Fig. 6). Nonetheless PBE-1 has better agreements for both short and large ^1H δ-shifts regions, making of LC-PBE xc functional the better functional to evaluate ^{13}C and ^1H δ-shifts of H_6EB. (2) The basis-set effect, QZVP and 6-31G(d), over ^{13}C and ^1H δ is assessed using ultrafine grid (mPW91-1a and mPW91-1b$_1$, respectively). Thus, the linear correlation results of QZVP (see Table 8 and 9 and Fig. 6) shows better results than 6-31G(d) in both ^{13}C and ^1H δ-shifts at the large region (see Tables 8 and 9), but not for the ^{13}C and ^1H-shifts in the short region showing a relative better agreement when 6-31G (d) is considered, in spite of this and considering that the differences between QZVP and 6-31G(d) are minimal in this region, it makes QZVP an appropriated basis set for the ^{13}C and ^1H δ-shift calculation. (3) The grid effect is also appraised, result for the fine grid from mPW91-1b and ultrafine grid from mPW91-1b1 shows similar values in all ^{13}C and ^1H δ regions, making of the use of ultrafine grid unnecessary to calculate the ^{13}C and ^1H δ of H_6EB structure-1.

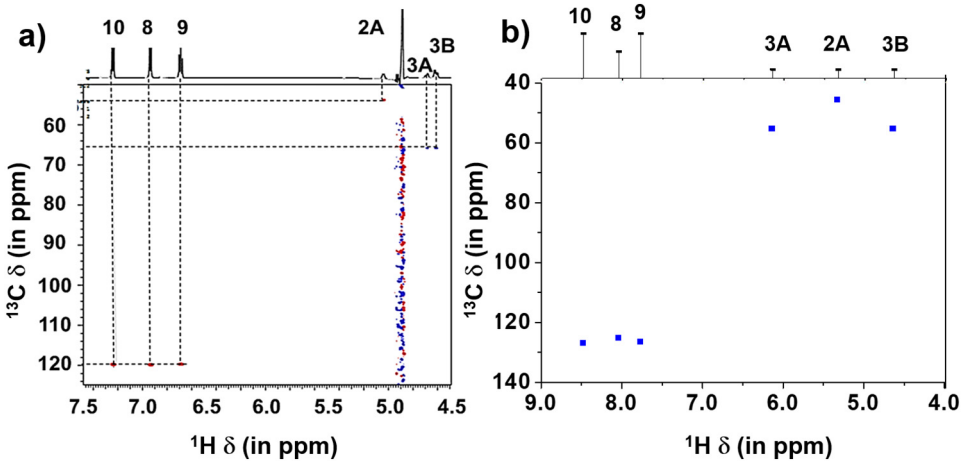

Fig. 4. H_6EB ^{13}C-^1H 2D–NMR spectra: (a) Experimental ^{13}C-^1H 2D–HSQC NMR spectra and (b) calculated NMR spectra by DFT (PBE-1).

Table 4
Experimental ^{13}C and ^{1}H chemical shifts (ppm) of H_6EB structure-1.

Labels	^{13}C[a]	^{1}H m (J [Hz])	^{13}C[a]	^{1}H m (J [Hz])
	Solvent: CD_3OD		Solvent: DMSO-d_6	
1	n.d.	–	169.4	–
2	53.7	5.04 m	51.2	4.90 ddd (9.1/7.0/4.4)
3	65.8	4.69 dd (11.5/3.1) 4.61 dd (11.5/5.8)	63.3	4.64 dd (11.0/9.1) 4.39 dd (11.0/4.4)
4	170.7	–	168.8	–
5	116.8	–	115.2	–
6	149.7	–	148.6	–
7	147.2	–	146.1	–
8	119.8	6.94 dd (7.9/1.4)	119.2	6.96 dd (7.9/1.3)
9	119.6	6.69 dd (8.2/7.9)	118.4	6.74 dd (8.3/7.9)
10	119.7	7.24 dd (8.2/1.4)	118.2	7.34 dd (8.3/1.3)
NH	–	(exchanged)	–	9.09 d (7.0)
6-OH	–	(exchanged)	–	11.61 s
7-OH	–	(exchanged)	–	9.40 s

[a] Chemical shifts of HSQC and/or HMBC correlation peaks; n.d. = not detected

Table 5
Calculated ^{13}C and ^{1}H chemical shifts (ppm) of H_6EB structure-1.

Name	PBE-1		mPW91-1a		mPW91-1b		mPW91-1b$_1$	
Labels	^{1}H δ	^{13}C δ	^{1}H δ	^{13}C δ	^{1}H δ	^{13}C δ	^{1}H δ	^{13}C δ
1		178.65		172.73		149.41		149.42
2	5.33	45.55	5.48	53.65	4.41	41.59	4.40	41.59
3A	6.14	55.18	5.80	63.41	4.95	51.09	4.95	51.11
3B	4.64	55.18	4.24	63.41	3.61	51.09	3.61	51.11
4		177.00		170.10		146.48		146.51
5		125.03		120.60		101.87		101.89
6		143.40		150.90		128.18		128.20
7		149.32		14808		125.19		125.16
8	8.04	125.07	7.70	126.31	6.81	106.86	6.81	106.89
9	7.77	126.47	7.37	122.80	6.54	103.69	6.54	103.67
10	8.48	126.79	8.00	125.61	7.03	106.35	7.03	106.33
6-OH	11.19		10.97		8.46		8.48	
7-OH	9.32		7.31		5.93		5.93	
N-H	8.35		7.51		5.83		5.83	

In general, comparing PBE-1 with all mPW91-1, we can emphasize that; the major difference arouses in ^{1}H δ region, indeed PBE-1 follow the same tendency that its experimental counterpart (with the exception of 3A δ-shifts), in comparison to the shifts for each mPW91 of N-H, 6-OH and 7-OH. The ^{1}H shifts for 2, 3B, 8, 9 and 10 δ regions have a better linear correlation when H-3A is not considered in the graphic, showing a slope and correlation factor (R^2) of 0.761 and 0.999, respectively, and an SD of 0.028 (see Fig. 7b and Table 9) than all mPW91-1 results (see Table 9). When the ^{1}H shift for H-3A is considered in the chart formulation, these values change to 0.803, 0.928 and 0.398, respectively.

The effects of xc-functional, basis set and grid of the calculated ^{1}H and ^{13}C chemical shifts for the H_6EB structure-2 evaluated and compared with experimental results (shown in Table 6), are also assessed in three steps; (1) The effect of xc-functional is evident, PBE-2 shows a better agreement in the short ^{13}C δ region and the large ^{1}H δ than the results for mPW91-2a, the comparison is different for the structure-1 (see Figs. 2 and 6, and Tables 8 and 9), therefore we can conclude that the chemical shifts of the H_6EB structures considered depend on the xc-functional used and the dihedral angles. (2) The change of large and small basis-set; QZVP and 6-31G(d), is also valuated in the structure-2 by mPW91-2a and mPW91-2b1 (see Fig. 6). The results showed in Tables 8 and 9 and Fig. 6 show that QZVP exhibit better results in short and large ^{13}C region and large ^{1}H δ region than 6-31G (d), which shows better result only in the short ^{1}H δ region, reinforcing that the use of large basis-set "QZVP" is appropriated to calculate ^{1}H and ^{13}C chemical shifts like we said above. (3) Like the structure-1, the grid effect on structure-2 is trivial and shows in both cases, mPW91-2b and mPW91-2b1, similar results (see Fig. 6).

Neither the use of fine or ultrafine grid or 6-31G(d) basis-set for mPW91-2 improve the assess obtained for PBE-2. Thus, in our case the xc LC-PBE functional in combination with the QZVP basis set using an ultrafine grid offer a better agreement than the other DFT methods tried. About the structures considered in the calculation, H_6EB structure-1 fit better than structure-2 when LC-PBE/QZVP DFT method with ultrafine grid is used as well as for all the performance of xc- mPW1PW91, showing clearly the dependence of the calculation method with the dihedral angles considered in H_6EB structure.

Similar occurs for all the xc- mPW1PW91 results, showing clearly the dependence of the calculation method with the initial dihedral angle considered for the H_6EB structures considered. The effect of the dihedral angles selected for different H_6EB structures is also evaluated, the results showed by the comparison between PBE-1, PBE-2, PBE-3, PBE-4 and PBE-5 in Tables 5, 6, 7, 8 and 9 and Fig. 6 permits to infer that given the diversity found, PBE-1 (arm-1, arm-2 and arm-3∠ N-C_4-C_5-C_6; − 24.93°, 19.50° and 127.90°) shows better results than those structures with a homogeneous dihedral angle. Nonetheless, considering that H_6EB might suffer at higher temperatures a dynamical change of the dihedral angles considered, in both solution and gas, the right assessment of the suitability of the applied calculation methods is by use of the

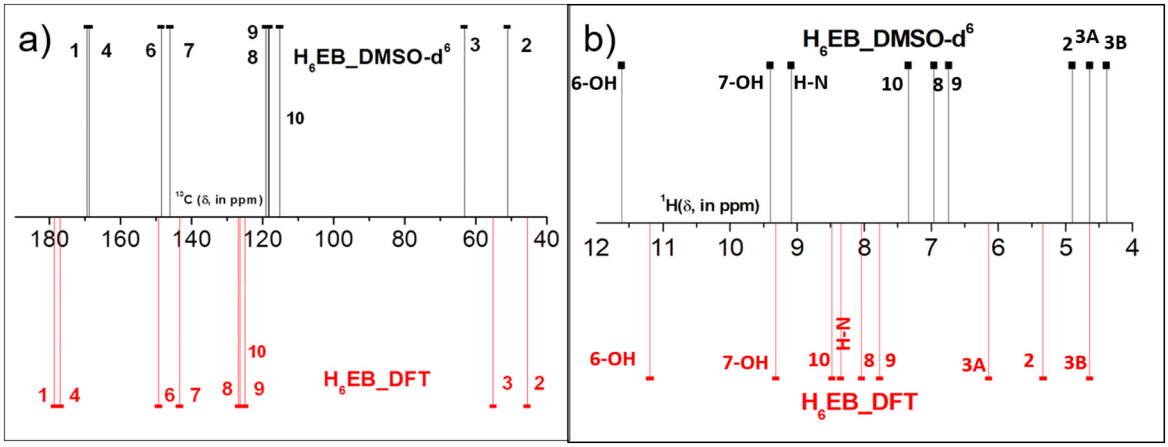

Fig. 5. Experimental (black) and PBE-1 (red) scheme of ^{13}C (a) and ^{1}H (b).

Table 6
Calculated ^{13}C and ^{1}H chemical shifts (ppm) for H_6EB structure-2 and 3.

Name	PBE-2		mPW91–2a		mPW91–2b		mPW91–2b$_1$		PBE-3	
Labels	^{1}H δ	^{13}C δ	^{1}H δ	^{13}C δ	^{1}H δ	^{13}C δ	^{1}H δ	^{13}C δ	^{1}H δ	^{13}C δ
1		193.66		171.82		148.89		148.86		188.97
2	5.37	56.27	5.52	53.31	4.48	41.96	4.49	41.93	4.85	57.30
3A	5.95	68.47	5.99	64.09	5.07	51.25	5.06	51.33	5.90	66.62
3B	4.30	68.47	4.02	64.09	3.47	51.25	3.46	51.33	5.28	66.62
4		184.25		167.08		144.22		144.20		192.04
5		138.63		123.65		103.71		103.71		123.79
6		158.51		150.96		128.54		128.54		169.55
7		155.74		144.44		121.63		121.64		160.63
8	7.41	139.47	7.65	125.96	6.61	106.26	6.61	106.30	6.60	132.48
9	7.37	137.34	7.48	121.67	6.56	102.90	6.56	102.90	5.95	132.55
10	8.78	146.35	8.58	131.41	7.56	112.36	7.57	112.37	6.65	132.14
6-OH	6.90		7.47		6.14		6.15		7.55	
7-OH	8.15		6.08		4.55		4.55		12.77	
N-H	9.37		8.47		6.71		6.70		7.55	

average of each structure here described and compared it with the other calculation methods, mpw91/QZVP and mpw91/6-31G(d), like showed in Tables 5, 6 and 7. It clearly shows that PBE/QZVP depicts a better DFT-method than mpw91/QZVP and mpw91/6-31G(d) as it is shown in Tables 8 and 9. Here, all chemical shifts calculated show a shift with respect to the experimental values; this behavior is expected, given the reasons described previously for the DFT methods used. Graphics of R^2, Slope and S.D. for large (a) and short (b) range of ^{1}H and ^{13}C δ using the different methods are provided in Figs. S2 and S3 of the SI.

The relationship between electrostatic potential (in range + 6.042E −2 and −6.042E−2 eV) and dihedral angles can be viewed in Fig. 8 for structure-1(a), structure-2 (b), structure-3 (c), structure-4 (d) and structure-5 (e), where spherical protrusions are generally individual atoms. Areas of low or partially low potential, red and yellow, are characterized by an abundance of electrons and are prone to react with positive or partially positive systems (positive part of a polar system). Areas of high potential, blue, tend to react with negative or partially negative systems (negative part of a polar system), they are characterized by a relative absence of electrons, being green regions neutral and therefore inactive or not susceptible to reactions. Oxygen has a higher electronegativity value than N. Oxygen atoms would consequently have a higher electron density around them than N, C and H atoms (H < C < N < O). Thus, the spherical region that corresponds to an oxygen atom has a red portion of it. Now note that there are three types of oxygen atoms in H_6EB; hydroxyls in catechol (yellow-red regions), carbonyl in amide (red-yellow regions) and ester groups in trilactone ring (red

Table 7
Calculated ^{13}C and ^{1}H chemical shifts (ppm) of H_6EB structure-4 and 5. An average of PBE/QZVP, mPW91/QZVP and mPW91/6-31G DFT-methods is as well provided.

Name	PBE-4		PBE-5		PBE (average)		mPW91-a$_1$ (average)		mPW91-b$_1$ (average)	
Labels	^{1}H δ	^{13}C δ	^{1}H δ	^{13}C δ	^{1}H δ	^{13}C δ	^{1}H δ	^{13}C δ	^{1}H δ	^{13}C δ
1		173.55		176.32		182.19		172.27		149.14
2	3.98	36.82	4.05	37.71	4.72	46.73	5.50	53.48	4.45	41.76
3A	5.01	47.87	5.11	49.21	5.62	57.47	5.89	63.75	5.01	51.22
3B	3.25	47.87	3.52	49.21	4.20	57.35	4.13	63.75	3.54	51.22
4		174.24		165.21		178.55		168.59		145.36
5		103.38		113.50		120.86		122.13		102.80
6		144.67		138.77		150.98		150.93		128.37
7		141.69		134.62		148.40		146.26		123.40
8	6.99	117.74	5.86	111.22	6.98	125.20	7.68	126.14	6.71	106.59
9	6.10	118.34	6.48	116.21	6.73	126.18	7.43	122.23	6.55	103.28
10	5.18	110.97	8.17	124.70	7.45	128.19	8.29	128.51	7.30	109.35
6-OH	11.77		4.92		8.47		9.22		7.31	
7-OH	5.76		2.48		7.70		6.70		5.24	
N-H	5.94		9.28		8.10		7.99		6.26	

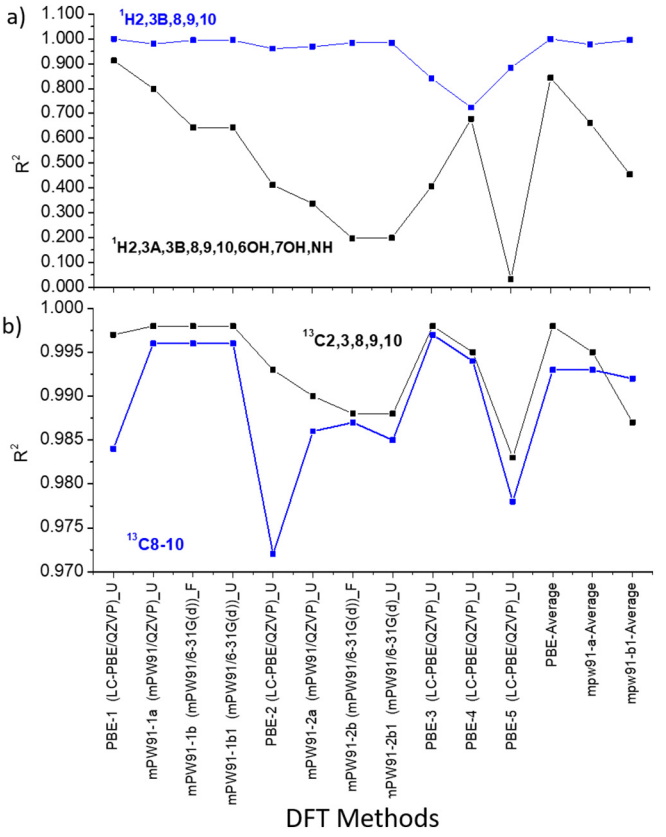

Fig. 6. R^2 of DFT methods of ^{1}H (a)and ^{13}C δ (b).

regions). The blue tainted sphere at the bottom corresponds to the location of the H atom and green to C atoms. The effect of dihedral angles on the reactive regions is evident, being the lowest potential region (prone to react with positive systems); amide group for the structure-1 (Fig. 8a), amide and ester groups for the structure 2 (Fig. 8b), hydroxyls for structure 3 (Fig. 8c), ester for the structure-4 (Fig. 8d), and amide and ester groups for the structure-5 (Fig. 8e), like specifies in Fig. 8f in range −6.0E−2 and −6.042E−2 eV and reveals the most reactive region prone to react with positive region (red).The electrostatic potential of some catecholamide arms of structure-1, structure-2 and structure-5 show similar distribution that catecholamide arm in tren(CAM)3, tren $(CAM)_2$1,2(HOPO) and other synthetic analogues of H_6EB reported by K. N. Raymond in 2008 [12]. Nevertheless, our study reveals a strong dependency of H_6EB properties with dihedral angles of catecholamide arms, specifically the electrostatic potential which disclose the inhomogeneous distribution of reactive sites in C3-symetric triscatecholamide, which affect their spectroscopic and donor-acceptor properties as is depicted in Fig. S8, in the analysis of frontier molecular orbitals of H_6EB structures.

Thus, instead K. N. Raymond in 2008 [12] study, in this contribution the steric effect is shown between the arms of catecholamide and these with the trilactone backbone by the evaluation of electrostatic potential and frontier orbital. This suggests that these reactive regions, where the delocalization of electrons (amide, esters and catechol groups) is predominant, are like a protein recognition code, giving rise to cellular memory. However, this is beyond the scope of this article.

H_6EB properties depend on the polarizability of the molecule; dynamic response of dipole moment of a bound system to external fields. In this context, we use MD simulations to evaluate the behavior of the dihedral angles of the solvated H_6EB molecule in a time lapse. For this, we consider four structures (structures 2, 3, 4 and 5). Although these structures correspond to the same molecule, each molecule contains different values of the dihedral angles on catecholamide. In this way,

Table 8
Calculated and experimental ^{13}C δ linear correlation results (statistical data).

Name	$^{13}C_{1-10}$			$^{13}C_{2,3,8,9,10}$		
	Linear correlation	R^2	S.D.	Linear correlation	R^2	S.D.
PBE-1	y = 0.890x + 10.323	0.984	5.35	y = 0.813x + 16.204	0.997	2.04
mPW91-1a	y = 0.993x − 2.656	0.996	2.58	y = 0.926x + 2.970	0.998	1.77
mPW91.b	y = 1.108x + 4.298	0.996	2.70	y = 1.036x + 9.190	0.998	1.59
mPW91-1b_1	y = 1.108x + 4.300	0.996	2.70	y = 1.036x + 9.173	0.998	1.59
PBE-2	y = 0.889x − 0.690	0.972	7.03	y = 0.777x + 8.928	0.993	3.38
mPW91-2a	y = 1.006x − 4.287	0.986	4.93	y = 0.901x + 4.583	0.990	3.85
mPW91-2b	y = 1.109x + 4.294	0.987	5.18	y = 1.005x + 10.700	0.988	4.27
mPW91-2b_1	y = 1.120x + 2.909	0.985	5.18	y = 1.005x + 10.682	0.988	4.26
PBE-3	y = 0.869x + 4072	0.997	2.31	y = 0.874x + 2.955	0.998	1.66
PBE-4	y = 0.858x + 21.58	0.994	3.31	y = 0.835x + 21.95	0.995	2.81
PBE-5	y = 0.890x + 17.93	0.978	6.23	y = 0.820x + 22.08	0.983	5.10
PBE	y = 0.886x + 9.818	0.993	3.59	y = 0.826x + 14.126	0.998	1.94
Average						
mpw91-a-Average	y = 1.000x − 3.608	0.993	3.66	y = 0.915x + 3.670	0.995	2.67
mpw91-b_1-Average	y = 1.115x + 3.462	0.992	3.85	y = 1.082x + 6.120	0.987	2.81

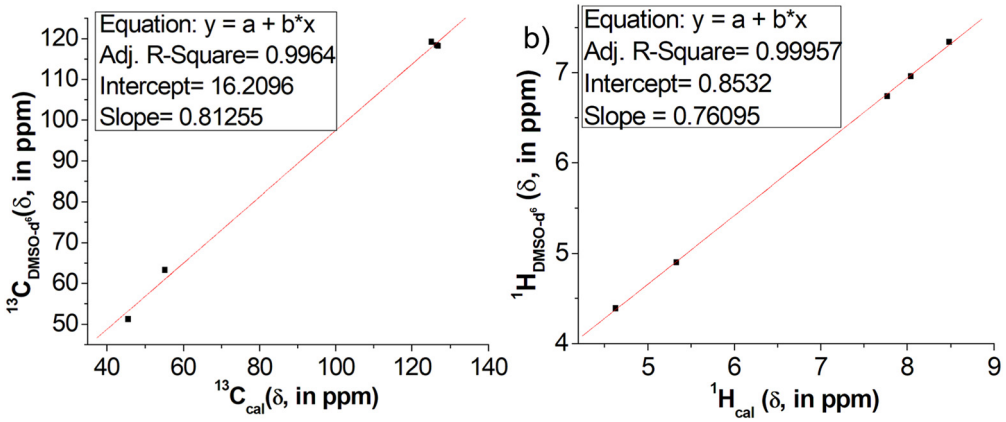

Fig. 7. $^{13}C_{DMSO\text{-}d6}$ and $^{13}C_{PBE\text{-}1}$ linear correlation ($^{13}C_{DMSO\text{-}d6} = 0.813\ ^{13}C_{PBE\text{-}1} + 16.21$), and (b) $^{1}H_{DMSO\text{-}d6}$ and $^{1}H_{PBE\text{-}1}$linear correlation ($^{1}H_{DMSO\text{-}d6} = 0.761\ ^{1}H_{PBE\text{-}1} + 0.853$).

we could consider that each MD simulations system is a replica, so we perform 4 replicas for this study. The values of the dihedral angles for each H_6EB structure were calculated. Additionally, we calculate the frequency distributions of the values of the dihedral angles for structure considering arm-1, arm-2 and arm-3 of structure-2, structure-3, structure-4 and structure-5 respectively (see Figs. S4–S7 in SI). The frequency distribution of values of dihedral angles in H_6EB structures exhibited a concentration of entries between −60 and 60° for all catecholamide arms, driving to structure-1 and structure-2 and structure-5 (see Table 2) as the predominant H_6EB structures. Therefore, is expected that the dihedral angles influence the properties of siderophores and their analogs like it is reported by Vonlanthen D. et al. [35] for a study of molecular conductance in a series of eight biphenyldithiols with fixed dihedral angles.

Table 9
Calculated and experimental ^{1}H δ linear correlation results (statistical data).

Name	$^{1}H_{2,3A,3B,8,9,10,6OH,7OH,\ NH}$			$^{1}H_{2,3B,8,9,10}$		
	Linear correlation	R^2	S.D.	Linear correlation	R^2	S.D.
PBE-1	y = 1.093x − 1.279	0.913	0.77	y = 0.761x + 0.853	1.000	0.028
mPW91-1a	y = 1.150x − 0.995	0.798	1.17	y = 0.808x + 0.768	0.980	0.22
mPW91-1b	y = 1.329x − 0.685	0.643	1.56	y = 0.848x + 1.248	0.995	0.11
mPW91-1b_1	y = 1.325x − 0.659	0.643	1.56	y = 0.848x + 1.253	0.995	0.11
PBE-2	y = 0.958x + 0.457	0.412	2.01	y = 0.727x + 1.235	0.961	0.78
mPW91-2a	y = 0.944x + 0.807	0.337	2.13	y = 0.709x + 1.355	0.969	0.27
mPW91-2b	y = 0.807x + 2.641	0.197	2.34	y = 0.776x + 1.613	0.984	0.19
mPW91-2b_1	y = 0.810x + 2.624	0.198	2.34	y = 0.776x + 1.615	0.984	0.20
PBE-3	y = 0.664x + 2.572	0.406	2.02	y = 1.529x − 2.901	0.842	0.61
PBE-4	Y = 0.825x + 2.279	0.678	1.49	y = 0.744x + 2.273	0.724	0.81
PBE-5	y = 0.201x + 6.117	0.032	2.57	y = 0.663x + 2.34	0.884	0.52
PBE average	y = 1.496x − 2.738	0.844	1.03	y = 0.910x + 0.560	1.000	0.03
mpw91-a-Average	y = 1.258x − 1.551	0.661	1.52	y = 0.757x + 1.064	0.978	0.23
mpw91-b1-Average	y = 1.244x − 0.006	0.454	1.94	y = 0.815x + 1.412	0.995	0.11

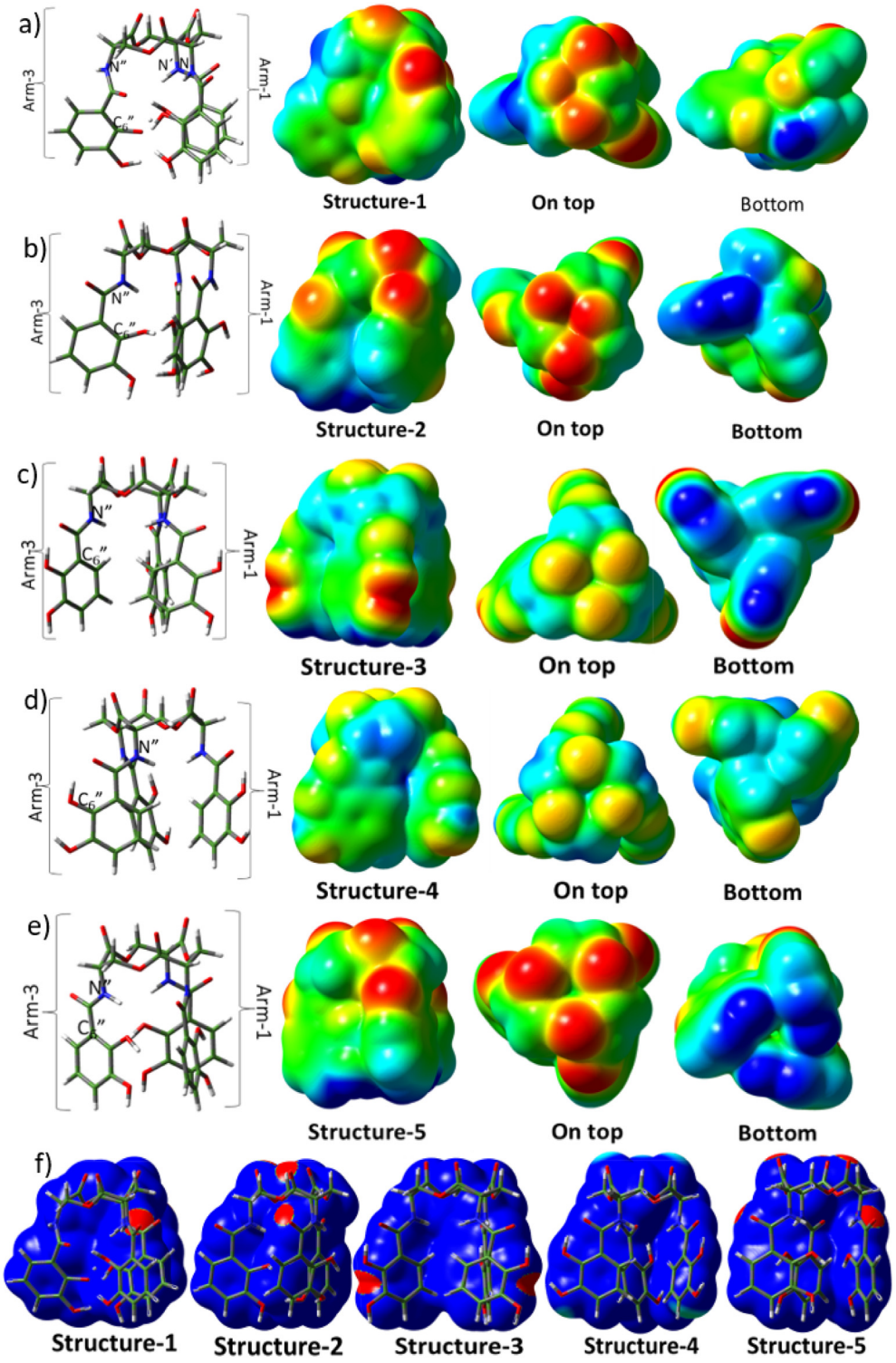

Fig. 8. Electrostatic potential maps from total SCF density of structure 1 (a), structure-2, structure-3, structure-4 and structure-5 in range + 6.042E−2 and −6.042E−2 eV (a–e), and in range − 6.0E−2 and −6.042E−2 eV (f).

4.3. H_6EB IR Spectra

We utilized high-quality experimental H_6EB IR obtained at 50000 scans in order carry-out linear correlation with calculated results, experimental H_6EB IR at different scans (from 1000 to 50000) is shown in Fig. S9 in SI. We used the average between PBE-1, PBE-2, PBE-3. PBE-4, PBE-5 (PBE xc-functional, QZVP basis set and ultrafine grid) to obtain more information about the H_6EB-IR bands within all MID-IR regions (see Figs. 9–12, Tables 10, 11 and 12). Indeed, the assignation of these bands is easier to obtain with computational support for most of the functional groups; for example, the broad band localized at 3420 cm^{-1} often attributed to the overlap between OH and NH [36]. In our calculation, however, the IR spectra clearly shows that this broad band belongs to the overlap of three OH stretching modes,

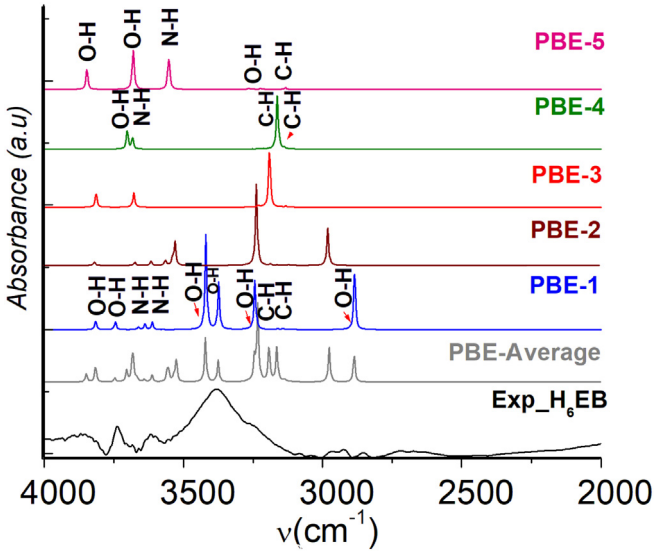

Fig. 9. Experimental and PBE-1-5 and PBE-average H_6EB-IR spectra within the range of 4000–2000 cm^{-1}.

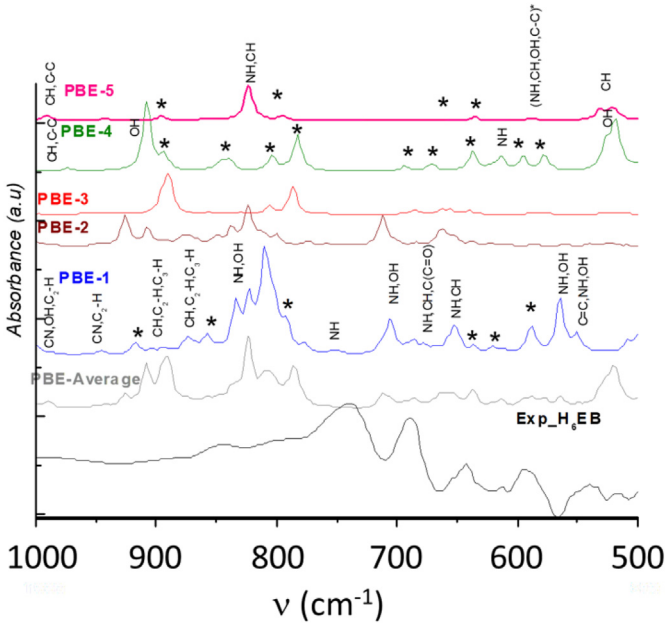

Fig. 11. Experimental and PBE-1-5 and PBE-average H_6EB-IR spectra within the range of 1000–500 cm^{-1}.

which are NH stretching bands located at higher frequencies, showing three discernible medium-sharp bands, each belongs to individual catechol amide arm.

Two others OH stretching bands seen at 3775.04 and 3814.13 cm^{-1}, are identified in the experimental IR spectrum to the bands at 3741.04 and 3811.75 cm^{-1}, respectively (detailed animated vibrations in SI). Note that such bands are strongly influenced by the formation of hydrogen bonds from the interaction with solvents. Some shifts of N-H IR bands can be a result of the proton transfer to the neighboring oxygen like was reported by Ushakumari et al. [37].

Below 3100 cm^{-1}, it is possible to observe several bands that correspond to asymmetric and symmetric stretching modes of C—H (from methyl group). The most typical are those localized at 2852.25, 2929.15 and 2965.93 cm^{-1} in the experimental IR of alkane groups.

Generally, in our calculations all theoretical peaks in this region show a good linear agreement with the experimental frequencies (see Fig. 13), with a slope and correlation factor of 1.081 and 0.980, respectively, and SD of 49.85 cm^{-1} (see Table 13). Similar differences were reported in an experimental study of the molecular structure of DL-serine using low-temperature IR spectroscopy by E. V. Korolik et al [38]. Our results prove that the similarity of the calculation frequency with the experimental results enables the correct assignment of experimental bands in this region.

At higher frequencies, such as those at 3039.91, 3079.62 and 3160.80 cm^{-1}, the bands shift to higher frequencies in the theoretical spectra, as shown in Table 10. All these bands correspond to asymmetric and symmetric stretching of C3—H, C3′—H, C3″—H and C2—H, C2′—H, C2″—H, the number of bands are a result of the asymmetry in the crown ester of H_6EB. Yi Li et al. [16] reported, and it is generally well known, that shifted C—H bands result from ignoring the Fermi resonance in

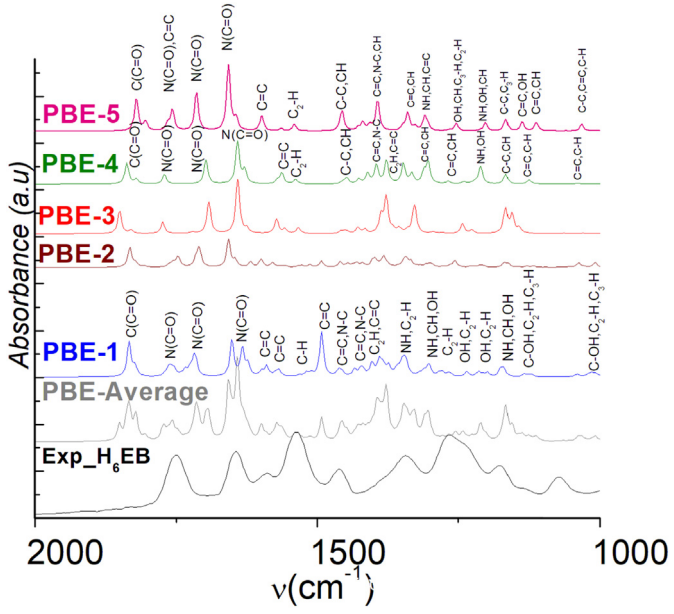

Fig. 10. Experimental and PBE-1-5 and PBE-average H_6EB-IR spectra within the range of 2000–1000 cm^{-1}.

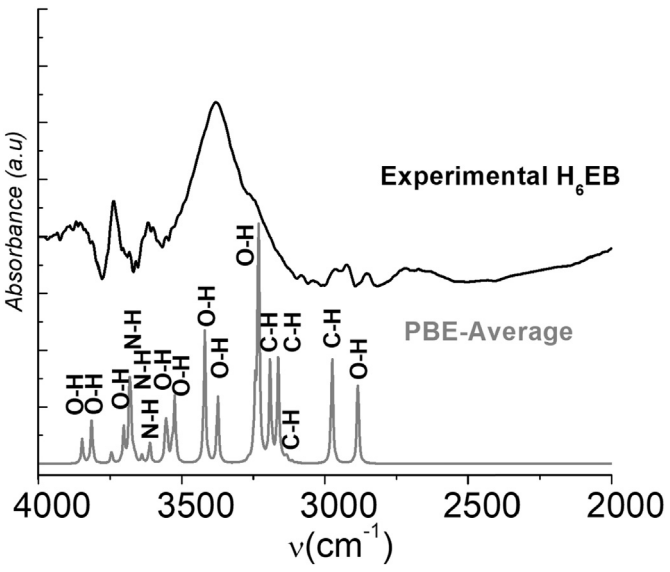

Fig. 12. Experimental and average PBE H_6EB-IR spectra within the range of 4000–2000 cm^{-1}.

Table 10
Experimental and calculated IR spectra of H_6EB within the range of 2000–4000 cm^{-1}.

Band assignment	PBE-1	PBE-2	PBE-3	PBE-4	PBE-5		PBE -Average in cm^{-1}		Exp IR in cm^{-1}	
O—H	2884.78	2974.45					2880.91		2720.76	
C_2—H	3097.67								2852.25	
C_2—H, C_3—H	3112.49								2929.15	
C_2—H, C_3—H	3131.56								2965.93	
C_2—H, C_3—H	3138.92								3039.91	
C_2—H, C_3—H							2973.56		3079.62	2973.37[a]
C_2—H, C_3—H	3145.4		3131.98	3163.11	3133.07					
	3160.8		3190.42		3142.71	3162.68	3161.60		3151.93	
					3212.27					
O—H	3243.64	3232.10			3222.36		3192.41			
					3248.04	3245.17	3230.32	3221.52	3245.97	
					3265.11		3241.84			
O—H	3373.86						3371.26		3383.49[a]	
O—H	3419.78	3526.23			3554.9		3420.68		3556.42[a]	
		3558.65					3522.30			
N—H	3612.25	3610.51					3611.72		3604.28	
	3638.72						3636.55	3624.14	3617.6	3619.28[a]
									3635.95	
N—H	3662.34	3668.38	3699.12	3683.27	3681.9		3676.18	3690.27	3663.29	3684.28[a]
							3704.36		3684.22	
									3705.17	
O—H	3775.04			3702.55			3747.59		3741.33	
O—H	3814.13	3812.44	3812.10		3846.15		3812.18		3811.75	
							3846.20			

[a] Average.

Table 11
Experimental and calculated IR spectra of H_6EB within the range of 1000–2000 cm^{-1}.

Band assignment	PBE-1		PBE-2	PBE-3	PBE-4	PBE-5	PBE- Average in cm^{-1}	Exp H_6EB in cm^{-1}	
C—OH, C—H	1040.44		1008.47		1039.42	1032.11	1031.77	1072.309	
			1038.43						
C—OH, C_2—H, C_3—H	1123.23		1118.15		1127.45	1113.36	1124.99	1134.169	
			1130.14			1137.61			
C—OH	1169.83	1181.15[a]	1170.45	1166.24	1166.15	1166.64	1174.80	1176.59	
C_2—H, C_3—H, N—H, C—OH	1175.39					1198.15			
C—OH, C_{ar}—-H	1198.24								
C_{ar}—H	1213.74	1224.43[a]	1212.26		1239.97		1235.19	1236.78	
δ_{ar}—H, C—OH	1235.12		1230.13		1269.17				
C_2—H in the plane deformation	1266.91	1272.79[a]	1256.69	1242.93		1253.31	1256.43	1264.99	
C═C	1278.67								
N—H, OH, C_{ar}—H,	1303.45	1332.90[a]	1302.42	1328.26	1303.32	1309.74	1336.54	1343.36	
C═C, N—H, OH, C_{ar}—H,	1345.16		1344.11	1380.29	1330.84	1339.82			
N—H, C_2—H, C═C	1350.09		1382.11		1348.08				
N—H, C_2—H, C_3—H	1373.26	1396.55[a]	1400.92	1428.62	1377.47	1393.48	1407.78	1390.18	
C_2—H	1390.35		1430.53		1395.05	1406.58			
C_2—H, C═C	1403.57				1410.68	1418.93			
C═C, C—N N—C_2	1418.64				1426.77				
C═C, N—C_2	1461.47	1476.91[a]	1460.57	1477.33	1447.68	1455.51	1468.44	1461.42	
C═C	1492.35		1492.62						
C_3—H	1511.18	1545.67[a]	1514.29	1533.55	1538.71	1540.78	1544.28	1538.35	
C_3—H	1519.6		1532.20	1572.13	1562.95				
C_3—H	1532.01		1558.20						
C═C	1566.14								
C═C	1569.5								
C═C	1575.63								
C═C	1582.44	1590.68[a]	1580.49			1564.81	1587.15	1588.92	
C═C	1590.19		1600.83			1598.96			
C═C	1599.4								
N—(C═O— (amide)	1632.96	1642.31[a]	1620.53	1637.24	1628.96	1644.46	1651.99	1644.31	
N—(C══O)—- (amide)	1651.65		1656.25	1693.29	1641.57	1657.63			
					1697.66				
N—(C═O)— (amide)	1715.51	1741.25[a]	1710.20	1721.22	1771.43	1714.81	1742.61	1750.26	
N—(C═O)— (amide)	1734.41		1750.88	1774.10		1756.98			
N—(C═O)— (amide)	1763.2								
C—(C═O)— (ester)	1818.12	1825.19[a]	1834.18	1841.34	1821.20	1805.53	1829.83	1817.34	1836.71[a]
C—(C═O)—(ester)	1823.5			1852.19	1837.98	1821.01		1835.11	
C—(C═O)—(ester)	1833.94							1857.68	

[a] Average

Table 12
Experimental and calculated IR spectra of H_6EB within the range of 500–1000 cm^{-1}.

Band Assignment	PBE-1		PBE-2	PBE-3	PBE-4	PBE-5	PBE-Average in cm^{-1}	Exp H_6EB in cm^{-1}	
OH	508.04							514.69	
C—H	516.3							518.9	
	524.18								
	530.5								
	540.52							531.92	
	549.83				518.24	532.08		538.95	
C═C, O—H, N—H	560.56	536.81		577.65	528.36	519.837	535.5		526.11[a]
N—H and O—H	564.56								
C_{ar}—H,C═C	588.811	593.99			576.93	586.4	590.46	594.45	
					594.85	600.12			
C_{ar}—H,C═C	599.164								
	611.14	635.44	664.31	640.19	613.08	635.02	646.25	612.04	642.30[a]
	619.94			662.27	637.17	658.78		641.8	
	636.3				669.99			652.46	
N—H and C—H	652.433							662.9	
	657.42								
N—H, C_{ar}—H, —O—C═O	686.05	695.61	712.51	686.19	693.97	688.18	695.29	688.92	
N—H,O—H	705.18								
N—H	754.06	754.06					754.06	740.02	746.34[a]
								752.66	
N—H, O—H, C—H	776.91	793.27	822.72	805.36	782.51	796.41	800.68	797.91	
N—H, O—H	792				803.81				
C_{ar}—H, N—H, O—H	810.9								
δC_{ar}—H,N—H, O—H	858.273	858.273	878.23		839.38	822.45	848.94	845.56	
					846.37				
C_{ar}—H,C_2—H,C_3—H	873.432	895.47	908.36	890.99	893.89	895.66	898.78	888.61	
					908.33				
N—H,C_2—H,C_3—H	917.499								
δC_2—H, C—N	946.337	980.66	924.51		973.34	941.71	980.04	992.16	
			1008.47		1041.27	990.32			
C—N,O—H	1014.99								

[a] Average.

the calculations. This can be viewed only for C—H fundamental and overtone vibrations, causing a split and shift in the intensity of peaks with similar energies and identical symmetries. Table 10 shows the IR band assignment for the experimental result based on the calculated IR spectrum for the region between 4000 and 2000 cm^{-1}.

Fig. 14 depicts the comparison of the PBE-Average and the experimental IR spectra of H_6EB in the region between 2000 and 1000 cm^{-1}.

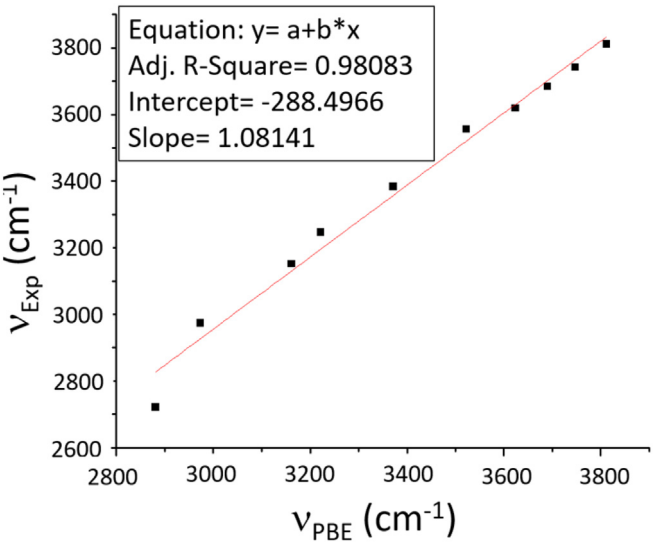

Fig. 13. ν_{solid} and ν_{PBE} Linear correlation of experimental and average PBE H_6EB-IR spectra ($\nu_{solid} = 1.081\nu_{cal} - 288.49$).

In their H_6EB-IR report published in 1983 [6], N. Raymond et al assigned the band localized at 1740 cm^{-1} the crown ester and the amide group based on the research of A. Hidalgo, H. Wilson and P. Wieklund [39–41] reported in 1960, 1974 and 1976, respectively, which used as aid the IR spectra of some carboxylic acid derivatives. As previously reported, the frequency of ester IR bands changes when it is forming a crown ester as in H_6EB, as it is in an open chain. In the study of carbonyls published in 2008 by J. Workman et al [43] reported that a more electronegative substituent will increase the carbonyl carbon oxygen stretch frequency by up to 100 cm^{-1} above the 1715 cm^{-1} nominal frequency. This was also confirmed in studies of some IR spectra of carboxylic acid derivatives and alpha-Angelica lactones, in which carbonyl stretching bands were localized at 1770 and 1818 cm^{-1} [42,44]. In the calculated IR spectra, this band can be seen at 1829.83 cm^{-1} with components at 1818.12, 1823.50 and 1833.94 cm^{-1}, which are similar to its experimental counterparts in the weak bands observed at 1817.34, 1835.11 and 1857.68 cm^{-1} (see Table 11). The experimental bands located at 1750.26, 1644.31 and 1588.92 cm^{-1} correspond exclusively to amide I, amide II and νC═C stretching mode, respectively. The bands at 1538.35 cm^{-1} and 1461.42 cm^{-1} belong to the overlaps of the C═C

Table 13
Calculated and experimental IR PBE-average linear correlation results (statistical data).

Region	IR PBE-average		
	Linear correlation	R^2	S.D.
4000–2000	y = 1.081x − 288.49	0.980	49.85
2000–1000	y = 0.976x + 38.06	0.997	12.83
1000–500	y = 1.017x − 15.69	0.998	7.13

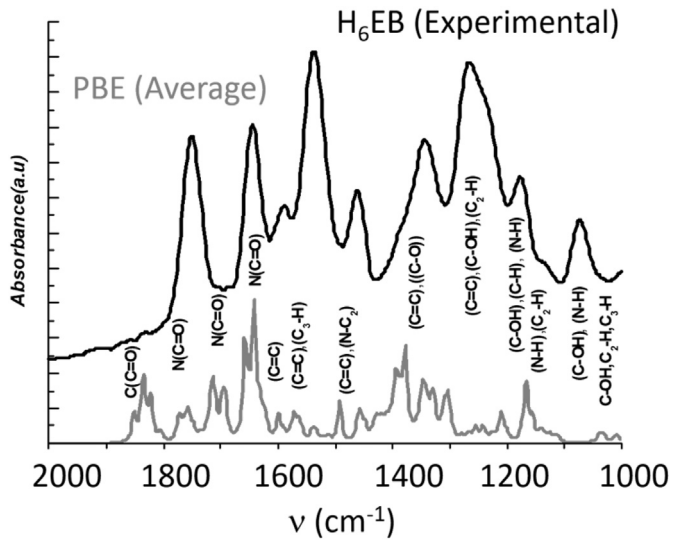

Fig. 14. Experimental and average PBE H_6EB-IR spectra within the range of 2000–1000 cm^{-1}.

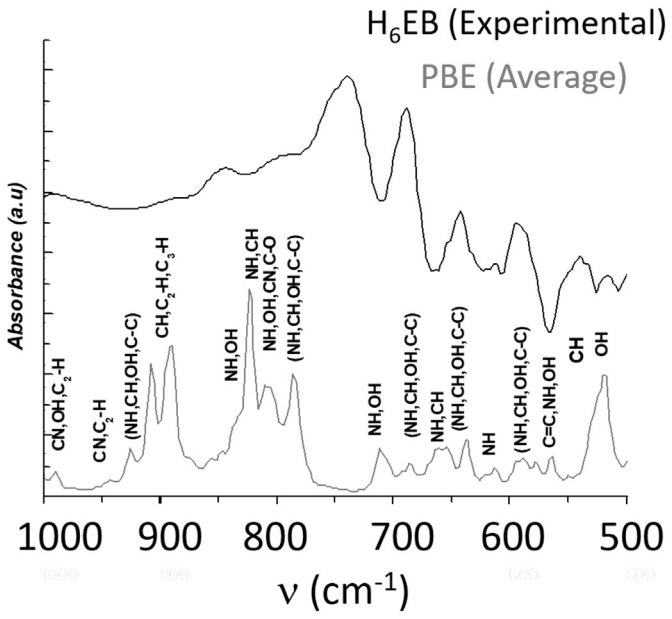

Fig. 16. Experimental and average PBE H_6EB-IR spectra within the range of 1000–500 cm^{-1}.

stretch and C—H bend and the C═C and C—N stretch (detailed animated vibrations in SI).

The next IR region (1420–1000 cm^{-1}) corresponds to the overlap between the stretching and bending regions, this overlap is reflected in the difficulty in their assignments. Here, the first bond named in each band corresponds to the largest vector contribution; thus, 1390.18, 1343.36, 1264.99, 1264.99, 1236.78 and 1776.59 cm^{-1} correspond to C═C, C—N stretching vibration, C2—H in the plane deformation, C—O and C—O stretching from catechol, which agrees with the findings of N. Raymond et al. [6]. The last two bands we have designed both have ν C—O + δ O—H.

Fig. 15 shows a linear correlation of the experimental and calculated H_6EB-IR spectra. All theoretical bands placed within this range (2000–1000 cm^{-1}) show a good linear correlation with the experimental frequencies (see Fig. 14), with a slope and a correlation factor (R^2) of 0.976 and 0.997, respectively, with an SD of 12.83 cm^{-1} (see Table 13). Table 11 summarizes the contribution of each band named here.

Fig. 16 depicts the H_6EB IR spectra in the range between 500 and 1000 cm^{-1}, which shows sixteen bands whose quantities are similar to the experimental spectrum; however, as reported by E. V. Korolik et al. [38], the bands in this region (specific to the bending modes) are prone to splitting and shifting when the temperature decreases, so their assignment is very difficult. We have grouped both theoretical and experimental bands to obtain eleven representative bands that correspond sequentially to C—C; N—H; Car—H; N—H; N—H with —O—(C═O)- contribution; N—H; O—H; O—H; C—N; Car-H with N—H contribution and C—N. Table 11 displays the assignments of the bands observed in this region. The average of both the experimental and theoretical bands placed in this range (1000–500 cm^{-1}) shows a good linear correlation with the experimental frequencies (see Fig. 16),

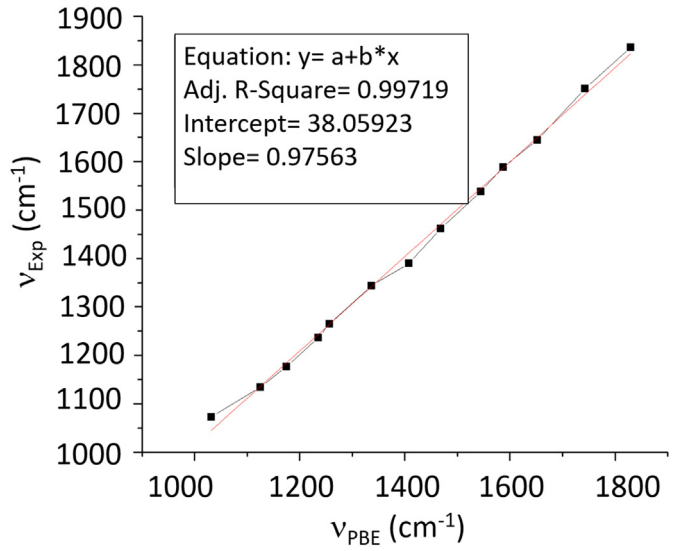

Fig. 15. ν_{solid} and ν_{PBE} linear correlation ($\nu_{solid} = 0.976\nu_{PBE} + 38.06$) of the experimental and calculated H_6EB-IR spectra.

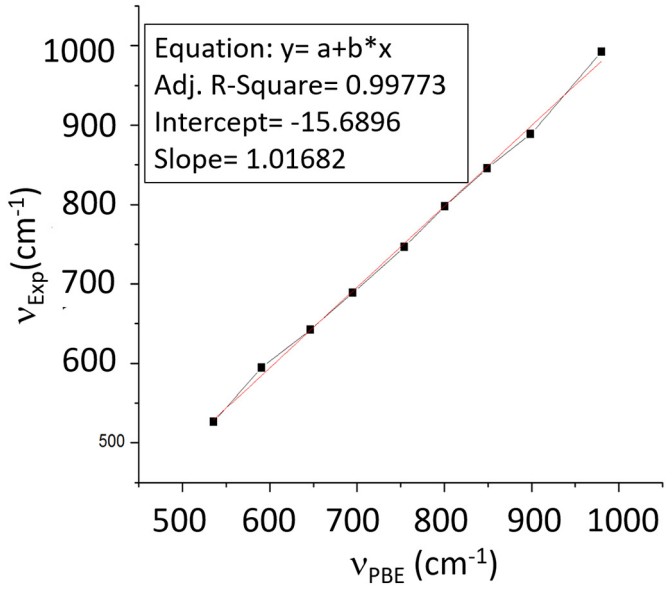

Fig. 17. ν_{solid} and ν_{PBE} linear correlation ($\nu_{solid} = 1.017\nu_{cal} - 15.69$) of the experimental and average PBE H_6EB-IR spectra.

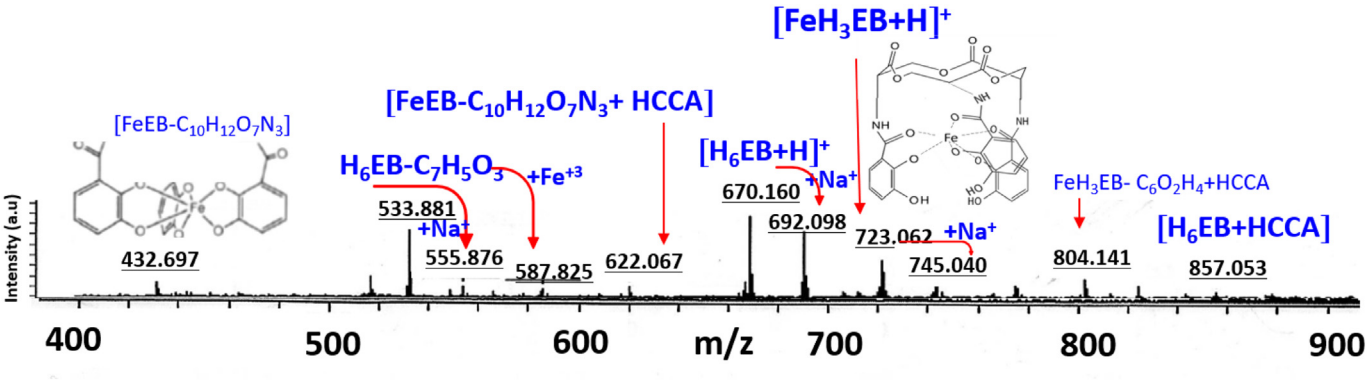

Fig. 18. MALDI-TOF MS spectra of $[FeH_3Enterobactin]^0$ (FeH_3EB).

with a slope and a correlation factor (R^2) of 1.017 and 0.998, respectively, with an SD of 7.13 cm^{-1} (see Fig. 17). The data here obtained, allows also to localize the N—H and O—H fingerprint regions (1500–400 cm^{-1}) and although it is complicated by the large number of different vibrational modes that occur here, and under the conditions in which the theoretical IR were performed (gas phase, low temperature), we can "highlight" that the calculated N—H and O—H finger prints at 1396.55, 1181.15, 895.47, 754.06 and 652.43 cm^{-1} corresponds exclusively to N—H, while 1332.90, 980.66, 793.27, 695.61 and 562.56 overlapped with OH bands and 1224.43, 1126.23, 1040.44, 858.27 cm^{-1} for OH bands, match with those reported for L-D serine and catechol group bands [16,6], see video SI. Experimental and calculated FeH_3EB IR was also performed of manner to support the suitability of this study. Figures from S10 to S12 in SI revel similitude between H_6EB and FeEB IR spectrums for both experimental and calculated. IR theoretical study of FeEnterobactin, with Fe, linked to different donor groups will be published elsewhere. FeEnterobactin (FeH_3EB) was purchased in Genaxxon Bioscience Gmbh and the measurement conditions for IR and MALDI-TOF-MS were similar to H_6EB.The utility of the IR calculation at solvent-free is that this offers an almost accurate correlation with experimental IR spectra which also is obtained using solvent-free environment, this allows predict the reactivity of H_6EB with chemical reagent in gas phase at room temperature by advanced processes of functionalization as those based on vapour phase metalation (VPM) process at room temperature.

4.4. FeH_3EB MALDI-TOF MS Spectra Analysis

Work in progress of the FeH_3EB compound shows (see spectrum displayed in Fig. 18) a good agreement for the most abundant isotope localized at 723.062 *m/z*, with a calculated value of 723.414 *m/z* for $[FeH_3EB + H]^+$, this allows iron to be designed in the triprotonated salicylate conformation (Fe linked at C4,4′,4″ and C6,6′,6″) rather than in the six-unprotonated catecholate conformation, with a calculated value of 719.382 *m/z* (Fe linked at C7,7′,7″ and C6,6′,6″), which is common in the liquid state. Similar catechols are linked to Fe, and a novel form of fragmenting is observed at 432.697 *m/z*, with a calculated value of 433.188 *m/z*; this is designated here as $[FeEB\text{-}C_{10}H_{12}O_7N_3]$, which considers the loss of the crown ester skeleton with the amide group, forcing Fe to move to C7–C6 rather than the C4–C6 position and changing its preference to the catecholate conformation. At 622.067 *m/z*, the existence of the same fragment mixture as HCCA can be confirmed, designated here as $[FeEB\text{-}C_{10}H_{12}O_7N_3 + HCCA]$, with a calculated value of 622.328 *m/z*. The expected cleavage is also seen at 587.825 *m/z* and 804.141 *m/z* with the loss of catechol and catechol + carbonyls groups, with calculated values of 587.301 and 804.492 *m/z* for $[FeH_3EB\text{-}C_7H_5O_3]$ and $[FeH_3EB\text{-}C_6H_5O_2]$, respectively. Details in Fig. S13 in SI.

5. Conclusions

MALDI-TOF MS spectra reveal a marked difference in the reactivity of H_6EB when matrix-assisted laser desorption/ionization-time is used. Specifically, we emphasize the fragmentation change when H_6EB is linked to iron, passing the incision selectivity since the amide group in H_6EB to C4 and C5 in FeH_3EB. This is rational considering that FeH_3EB contains Fe coordinated to O4,4′,4″ and O6,6′,6″. The results show significant differences between the O—H and N—H bands, and the C═O amide and O-(C═O) IR bands which are often on top of each other. The NMR DFT calculations reported here show a strong dependence of the exchange-correlation functional, basis set, grid and the dihedral angles considered in H_6EB structure. Thus, the good agreement between both IR and NMR spectra for the xc LC-PBE functional with QZVP basis set using ultrafine grid of both H_6EB structure-1 and average with the experimental results compared with the others DFT methods (mPW91/QZVP and mPW91/6-31G(d)) here utilized, in spite of the absence of solvent, our results allowed to consider that the calculated IR spectra and ^1H and ^{13}C chemical shifts form a reliable standard set for the spectroscopic characterization of Enterobactin systems.

Supplementary data to this article can be found online at https://doi.org/10.1016/j.saa.2018.02.060.

Funding Sources

Lamellar Nanostructure and BioNanomedicine groups of the Center for the Development of Nanoscience and Nanotechnology (CEDENNA) Chile, and the Max Planck Institute for Microstructure Physics. ACT-1107 Project titled "Integration of Structural Biology to the development of Bionanotechnology" funded by CONICYT Chile. FGN acknowledge the support of FONDECYT Grant 1170733 and MAA is funded by CONICYT PCHA/Doctorado Nacional 2017-21172039 fellowship. The Centro Interdisciplinario de Neurociencia.

Notes

This research began during M.A. Moreno's time in Dr. M. Knez's group at Experimental Department II of the Max Planck Institute for Microstructure Physics in 2011.

Acknowledgment

We thank Prof. Dr. Peter Fratzl, acting Director of the Experimental Department 2 from the Max Planck Institute of Microstructure Physics, Dr. M. Knez, from CIC-Nanogune and the Computer facilities of the Max Planck Institute for Microstructure Physics and the CBIB of Universidad Andres Bello.

References

[1] W.R. Harris, C.J. Carrano, S.R. Cooper, S.R. Sofen, A.E. Avdeef, J.V. McArdle, N.K. Raymond, J. Am. Chem. Soc. 101 (1979) 6097–6104.
[2] J.B. Neilands, Annu. Rev. Biochem. 50 (1981) 715–731.
[3] T. Klabunde, C. Eicken, J.C. Sacchettini, B. Krebs, Nat. Struct. Mol. Biol. 5 (1998) 1084–1090.
[4] P. Fratzl, M.J. Harrington, A. Masic, N. Holten-Andersen, J.H. Waite, Science 328 (2010) 216–220.
[5] K.N. Raymond, R.J. Aberget, J.A. Warner, D.K. Shuh, J. Am. Chem. Soc. 128 (2006) 8920–8931.
[6] K.N. Raymond, V.L. Pecoraro, W.R. Harris, G.B. Wrong, C.J. Serrano, J. Am. Chem. Soc. 105 (1983) 4623–4633.
[7] D.L. Stephens, M.D. Choe, C.F. Earhart, Microbiology 141 (1995) 1647–1654.
[8] K.N. Raymond, E.A. Dertz, S.S. Kim, PNAS 100 (2003) 3584–3588.
[9] S.K. Buchanan, B. Smith, L. Venkatramani, D. Xia, L. Esser, M. Palnitkar, R. Chakraborty, D. Van der Helm, J. Deisenhofer, Nat. Struct. Mol. Biol. 6 (1999) 56–63.
[10] R. Chakraborty, E.A. Lemke, Z. Cao, P.E. Klebba, D. Van der Helm, Biometals 16 (2003) 507–518.
[11] B. Herbert, Curr. Top. Med. Chem. 1 (2001) 73–82.
[12] K.N. Raymond, T.M. Hoette, R.J. Abergel, J. Xu, R.K. Strong, J. Am. Chem. Soc. 130 (2008) 17584–17592.
[13] K.N. Raymond, B. O'Sullivan, D.M.J. Doble, M.K. Thompson, C. Siering, J. Xu, M. Botta, S. Aime, Inorg. Chem. 42 (2003) 2577–2583.
[14] T. Baramov, K. Keijzer, E. Irran, E. Mösker, M.H. Baik, R. Süssmuth, Chem. Eur. J. 19 (2013) 10536–10542.
[15] G. Schreckenbach, Y. Ruiz Morales, T. Ziegler, J. Chem. Phys 104 (1996) 8605–8612.
[16] Y. Li, H. Zhang, Q. Liu, Spectrochim. Acta A Mol. Biomol. Spectrosc. 86 (2012) 51–55.
[17] D.H. Kim, H.M. Eun, H.S. Choi, Bull. Kor. Chem. Soc. 21 (2000) 148–150.
[18] G. Barone, P.L. Gomez, D. Duca, A. Silvestri, R. Riccio, G. Bifulco, Chem .Eur. J. 8 (2002) 3233–3239.
[19] J.P. Perdew, K. Burke, M. Ernzerhof, Phys. Rev. Lett. 77 (1996) 3865–3868.
[20] F. Weigend, R. Ahlrichs, Phys. Chem. Chem. Phys. 7 (2005) 3297–3305.
[21] F. Weigend, F. Furche, R. Ahlrichs, J. Chem. Phys. 119 (2003) 12753–12762.
[22] R. Ditchfield, W.J. Hehre, J.A. Pople, J. Chem. Phys. 54 (1971) 724–728.
[23] M.M. Francl, W.J. Pietro, W.J. Hehre, J.S. Binkley, M.S. Gordon, D.J. DeFrees, J.A. Pople, J. Chem. Phys. 77 (1982) 3654–3665.
[24] C. Adamo, V. Barone, J. Chem. Phys. 108 (1998) 664–675.
[25] J.P. Perdew, J.A. Chevary, S.H. Vosko, K.A. Jackson, M.R. Pederson, D.J. Singh, C. Fiolhais, Phys. Rev. B 46 (1992) 6671–6687.
[26] J.P. Perdew, K. Burke, M. Ernzerhof, Phys. Rev. Lett. 78 (1997) 1396.
[27] J. Am. Chem. Soc. 71 (1949) 1073–1079;
Gaussian 09, in: M.J. Frisch, et al., (Eds.), Rev. C.01, 2010 Wallingford CT.
[28] W.L. Jorgensen, J. Chandrasekhar, J.D. Madura, R.W. Impey, M.L. Klein, J. Chem. Phys. 79 (1983) 926–935.
[29] W.L. Jorgensen, D.S. Maxwell, J. Tirado-Rives, J Am Chem Soc 118 (1996) 11225–11236.
[30] Desmond Molecular Dynamics System, Version 3.6, D.E. Shaw Research, New York, NY, 2013.
[31] W. Humphrey, A. Dalke, K. Schulten, VMD: visual molecular dynamics, J. Mol. Graph. 14 (1996) (33 e38).
[32] M.E. Wieser, N. Holden, T.B. Coplen, J.K. Böhlke, M. Berglund, W.A. Brand, P. De Bièvre, M. Gröning, R.D. Loss, J. Meija, Pure Appl. Chem. 85 (2013) 1047–1078.
[33] M. Llinás, D.M. Wilson, J.B. Neilands, Biochemistry 12 (1973) 3836–3843.
[34] G. Schreckenbach, T. Ziegler, Theor. Chem. Accounts 99 (1998) 71–82.
[35] V. Vonlanthen, A. Mishchenko, M. Elbing, M. Neuburger, T. Wandlowski, M. Mayor, Angew. Chem. 48 (2009) 8886–8890.
[36] A. Shanzer, J. Libman, S. Lifson, C.E. Felder, J. Am. Chem. Soc. 108 (1986) 7609–7619.
[37] L. Ushakumari, H.T. Varghese, C.Y. Panicker, T. Ertan, I. Yildiz, J. Raman Spectrosc. 39 (2008) 1832–1839.
[38] E.V. Korolik, R.G. Zhbankov, A.A. Ivanov, G.K. Il'ich, N.I. Insarova, V.G. Leshchenko, Journal of App. Spectrosc 65 (1998) 906–910.
[39] A. Hidalgo, C. Otero, Spectrochim. Acta 16 (1960) 528–539.
[40] H.W. Wilson, Spectrochim. Acta A 30A (1974) 2141–2152.
[41] P.A. Wieklund, D.G. Brown, Inorg. Chem. 15 (1976) 396–400.
[42] R.N. Jones, C.L. Angell, T. Ito, R.J. Smith, Can. J. Chem. 37 (1959) 2007–2022.
[43] J. Workman, L. Weyer, Practical Guide to Interpretive Near-infrared Spectroscopy, CRC Press, 2007 71.
[44] R.S. Rasmussen, R.R. Brattain, J. Am. Chem. Soc. 71 (1949) 1073–1079.